Chemical Engineering Journal 450 (2022) 137935

Contents lists available at ScienceDirect

Chemical Engineering Journal

journal homepage: www.elsevier.com/locate/cej

Photocatalytic reduction of levulinic acid using thermally modified niobic acid

José B.G. Filho [a,*], Gustavo H.M. Gomes [a], Ingrid F. Silva [a,d], Regiane D.F. Rios [a], Henrique F.V. Victória [b], Klaus Krambrock [b], Marcio C. Pereira [c], Luiz C.A. Oliveira [a,*]

[a] Department of Chemistry, Federal University of Minas Gerais (UFMG), 31270-901 Belo Horizonte, MG, Brazil
[b] Department of Physics, Federal University of Minas Gerais (UFMG), 31270-901 Belo Horizonte, MG, Brazil
[c] Institute of Science, Engineering, and Technology, Federal University of Jequitinhonha and Mucuri Valleys (UFVJM), 39803-371 Teófilo Otoni, MG, Brazil
[d] Department of Colloid Chemistry, Max Planck Institute of Colloids and Interfaces, Am Mühlenberg 1, D-14476 Potsdam, Germany

ARTICLE INFO

Keywords:
Photocatalysis
Niobium oxide
Oxide defects
Biomass conversion
Oxygen vacancies
Structural defects

ABSTRACT

After the discovery that commercial niobic acid (H0) is able to reduce the levulinic acid in value added molecules, H0 was thermally treated at 200 °C, 400 °C, and 600 °C, generating the niobium oxides H1, H2 and H3 and the photocatalytic improvement towards reduction was investigated. Although the higher temperatures significantly decreased the specific surface area, it was important to remove surface hydroxyl groups and create the T and TT-Nb2O5 phase mixture in H3 which were responsible for its best performance (36.4% of conversion and almost 99% of selectivity for reduced products). To further improve the H3 photoactivity, an identical synthesis was performed in H_2 flow to produce oxygen vacancies in the structure of the new photocatalyst (H3OV). This simple modification method increased ~7% of products yield, which is the best photocatalytic result obtained for pure niobium oxides so far, and proved that it is possible to significantly increase photocatalytic performance without laborious modifications. The electronic and structural differences between H3 and H3OV were investigated by XRD Rietveld refinement, EPR, HR-TEM, DRS and SAED analyses.

1. Introduction

Levulinic acid (LA) is one of the most promising molecules derived from lignocellulosic biomass [1,2]. LA can be obtained directly through the dehydration of both furfuraldehyde and 5-hydroxymethylfurfural (HMF) [3,4]. Due to carboxyl and carbonyl functional groups, it is possible to synthesize various products with different applications, such as fuel additives, food flavorings, pesticides, polymeric precursors, green solvents, plasticizers, resins, and other platform molecules [5]. Although several methods transform this versatile compound, none is as promising and sustainable as heterogeneous photocatalysis [6–9].

Heterogeneous photocatalysis occurs when the semiconductor absorbs photons with equivalent or higher energy than that necessary to overcome the bandgap, promoting the transition of electrons (e^-) from the valence band (VB) to the conduction band (CB), leaving holes (h^+) in VB. The e^-/h^+ pairs can permeate the semiconductor's entire structure, and most of the time, they recombine and return their energy to the medium as photons and/or phonons. On the other hand, when the photogenerated charges reach the surface of the photocatalyst, they can react with adsorbed species; the h^+ oxidize electron donors and the e^- reduce electron acceptors [10].

The mechanism behind this technique may seem straightforward, but it is quite the opposite. When it involves organic molecules, the reactions take place via radicals that make the system extremely complex [11]. Furthermore, it is not easy to correlate the steady-state surface properties with the reaction path. Unlike many conventional catalytic systems, "photocatalytic sites" have a very short lifetime [12]. These are the main reasons behind the scarcity of articles focused on photocatalytic conversion and the mechanism assessment of versatile molecules such as levulinic acid [13].

Recently, some photocatalytic systems have been designed to add value to lignocellulosic biomass platform molecules, most of them based on TiO_2 [7,13,14]. Despite the good photocatalytic activity of TiO_2 (mainly for oxidation purposes, via photogenerated holes, because its conduction band energy level is not so negative [15,16]), its overrated application limits the knowledge about the potential of other promising semiconductors for this type of chemical transformation. The Nb_2O_5 is a semiconductor that has been gaining visibility in the heterogeneous

* Corresponding authors.
E-mail addresses: balenagabriel@gmail.com (J.B.G. Filho), lcao.ufmg@gmail.com (L.C.A. Oliveira).

https://doi.org/10.1016/j.cej.2022.137935
Received 26 April 2022; Received in revised form 16 June 2022; Accepted 3 July 2022
Available online 6 July 2022

photocatalysis literature [17–20]. On the other hand, little is known about its real photocatalytic performance in the pristine form because it is commonly applied along with cocatalysts or in heterojunction scheme. [10,21–23]. A recent study [24] has demonstrated that electrons in the conduction band of niobic acid can reduce LA into value-added molecules via the accumulated electron transfer technique (AET). However, as only niobic acid was used in the photocatalytic conversion of LA, the true potential for generating value-added products from this biomass platform molecule by niobium oxides remains unknown. Regarding this, the aim of the present work is to understand how different thermal treatments on niobic acid affect the crystalline and electronic structure of the resultant Nb_2O_5 and what is their influence on levulinic acid reduction AET photocatalysis.

2. Experimental

2.1. Synthesis of niobium oxide photocatalysts

Each niobium oxide was produced by weighing 3 g of niobium acid (HY-340, supplied by Companhia Brasileira de Metalurgia e Mineração, CBMM) into an alumina crucible and heated at 200 °C (sample H1), 400 °C (sample H2), and 600 °C (sample H3) at 10 °C min^{-1} under air atmosphere. After reaching the final temperature, the photocatalysts were kept under heating for 3 h. The original niobic acid was named H0. The most efficient material (H3OV) was also synthesized under the same conditions of H3, howerver in a 10 mL min^{-1} flow of 10% H_2 and 90% N_2 instead of the air atmosphere.

2.2. Characterization

2.2.1. General characterization

To analyze the textural properties of the photocatalysts, N_2 adsorption/desorption analysis was acquired at 77 K on a Quantachrome Quadrasorb SI apparatus. The samples were degassed at 150 °C under vacuum (0.5 Torr) for 20 h before the measurements (3P Instruments Masterprep degassing machine). The specific surface area (SSA) was calculated by the Brunauer−Emmett−Teller (BET) method and the pore size distribution by Density Functional Theory (DFT). Diffuse reflectance spectra were recorded on a Shimadzu UV–Vis spectrophotometer model 3550 in the 200 to 1400 nm spectral range. The long-range structural ordering was verified by X-ray powder diffractometry (XRD) using a Bruker D8 Advance diffractometer equipped with a scintillation counter detector with CuKα radiation ($\lambda = 0.15418$ nm) applying 2θ step size of 0.05° and counting time of 3 s per step. The Pair Distribution Function (PDF or G(r)) analysis was acquired from the XRD data, using a Python-based library called Diffpy.PdfgetX and the graphical interface was produced by the PDFgui software [25–27]. To understand the chemical environments of Nb oxides, Fourier-transform infrared attenuated total reflectance (FTIR-ATR) measurements were taken on a Varian1000 FT-IR spectrometer equipped with an attenuated total reflection diamond unit in the range of 550 to 4000 cm^{-1}.

2.2.2. Specific characterization

Further characterizations were made for the best photocatalyst of the H0-H3 series and its analog generated in the H_2 flow (H3OV). For these, X-ray photoelectron spectroscopy (XPS) measurements were carried out on Thermo Scientific K-Alpha equipment. The spectra were recorded using an Al-Kα X-ray source (400 μm-spot size), the survey spectra were collected with a pass energy of 200.00 eV and energy step of 1.000 eV. The Nb 3d and O 1 s were recorded with a pass energy of 50.00 eV and an energy step of 0.100 eV. Rietveld refinement from XRD data was performed using the GSAS/EXPGUI software to obtain crystallographic parameters and the phase percentages. High-resolution Transmission Electron Microscopy (HR-TEM) and Selected Area Electron Diffraction (SAED) images were taken on TECNAI G2-20 Super Twin FEI 200 kV to verify the short-range lattice order. Powder Electron paramagnetic resonance (EPR) measurements were performed on Magnettech MiniScope MS400 spectrometer operating at the frequency of 9.4 GHz (the X-band) at room temperature (~23 °C) and at low temperatures, using an Oxford Cryostat He-flow system apparatus, to detect paramagnetic defects in the niobium oxides.

2.2.3. Photocatalysis

Photocatalytic tests were performed in 15 mL flat-bottom quartz tubes purchased from Purshee Optical Elements Company (China). In each reactor, 20 mg of photocatalyst were weighed and 2 mL of 0.1 mmol mL^{-1} solution of LA in ethanol was added. Then, the reactors were sealed with a rubber septum. Molecular oxygen was removed from the system as follows: 10 min of ultrasound bath and 1 min of an intense flux of N_2 inside the headspace (using two needles, the input and the output). The reaction medium was subjected to 254 nm UV-C radiation (OSRAM PURITEC HNS S 11 W, GCF11DS/G23/SE/OF·G23, luminous intensity of 7800 cd) under magnetic stirring for 16 h. The parameters, such as solvent volume, mmol of LA and the mass of photocatalyst, were obtained from an optimization study made by our group specifically for this type of quartz reactors.

2.2.4. Molecular characterization

At the end of the reaction, 1 mL aliquots were extracted placed in a 1.5 mL vial, and injected into an Agilent 789B gas chromatograph instrument set with the following parameters: HP - INNOWAX column (30 m, 0.250 mm and 0.15 μm), He flow of 2 mL min^{-1}, 1 μL of injection volume, injector at 270 °C with a split ratio of 1:10, the temperature started at 40 °C and ended at 250 °C with a heating rate of 10 °C min^{-1}. The detector, Agilent 5977B MSD mass spectrometer, was set at 150 °C and performed the mass analysis in the scan mode, ranging from 20 to 300 *m/z*. The products were quantified according to reference [24].

2.2.5. Detection of radical species

To understand the radical nature of the best photocatalytic systems, spin trapping measurements were performed using the N-*tert*-Butyl-α-phenylnitrone (PBN - CAS 3376-24-7, 98%, TCI America, Japan − 100 mM ethanol solution) and 5,5-dimethyl-1-pyrroline N-oxide (DMPO - CAS 3317–61-1, 96%, Oakwood, EUA − 150 mM ethanol solution). The tests were carried out at room temperature, under similar conditions in which the photocatalytic reactions were performed. For this, 50 μL aliquots were withdrawn using a capillary glass tube and inserted inside quartz tubes after into the cavity of the same EPR spectrometer, in which the powders were analyzed. The spectra were identified through simulations performed by Easyspin [28].

3. Results and discussion

3.1. Characterization of niobium oxides

The niobium pentoxide (Nb_2O_5) crystallizes in different phases. In this work, the starting material, H0, is an amorphous $Nb_2O_5{\cdot}nH_2O$ at standard conditions [24]. It has been shown that at low calcination temperatures, the amorphous Nb_2O_5 crystallizes in TT-phase (pseudo-hexagonal) and it is favored by defects [29,30]. Fig. 1(a) shows the experimental XRD patterns of samples, along with the standard diffraction profile for the TT (CCDC#: 2103847) [31] and T (ICSD#: 1840) phases [32].

The H0, H1, and H2 samples showed poorly defined and broadened patterns, indicating that they are predominantly amorphous. On the other hand, the H3 has crystallinity, a TT and T phases mixture. The acronyms for TT and T come from the German words tief-tief and tief, which means “quite low” and “low” crystal phase calcination temperature [33], respectively. The TT and T phases present a similar structure, however, the TT has fewer niobium atoms in more symmetric Wyckoff positions, forming an orthorhombic superlattice [30,34]. An in-depth discussion about the differences and particularities of these crystalline

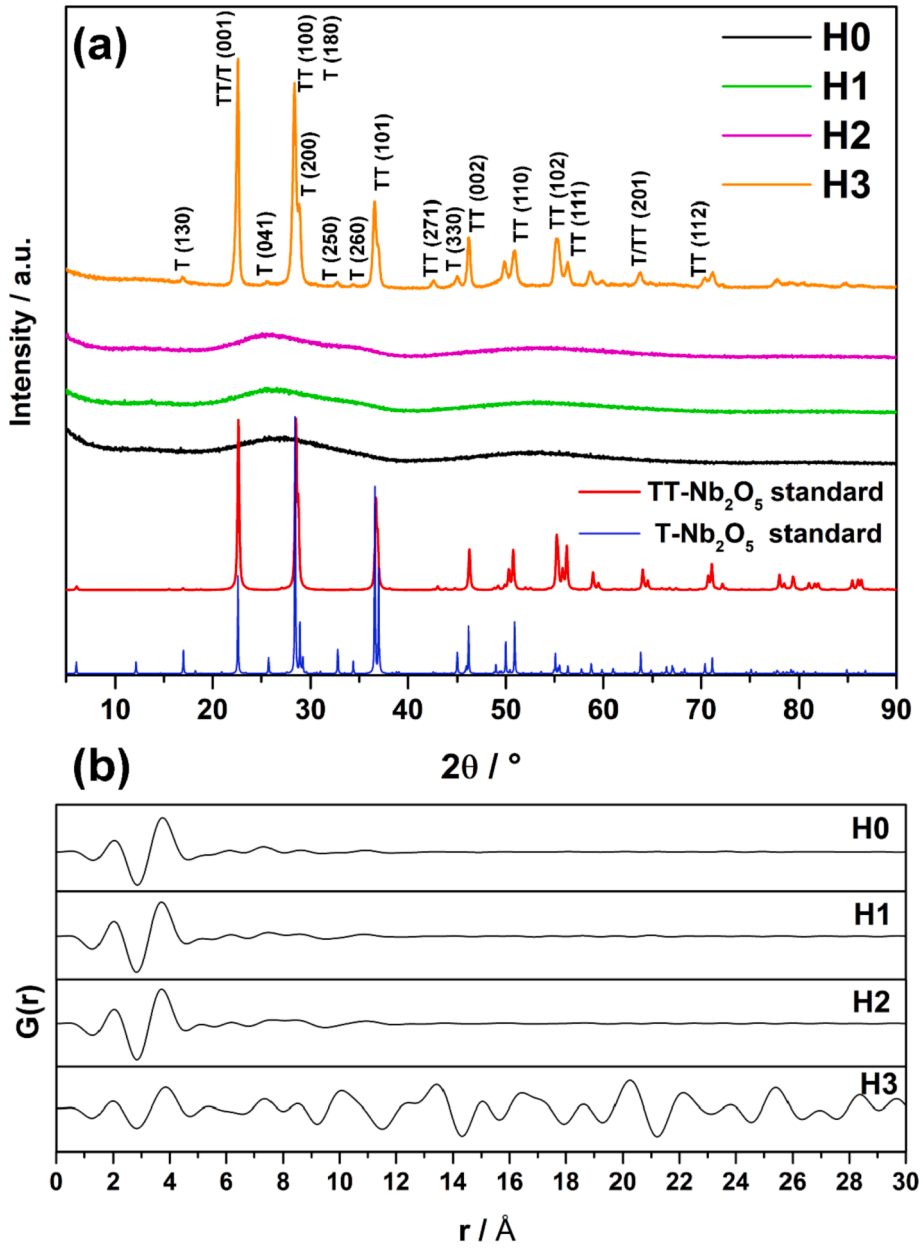

Fig. 1. **(a)** XRD patterns of the different niobium oxide photocatalysts **(b)** PDF analysis of the powder XRD.

phase can be found in the literature [35]. The H3 presented features of the TT-phase, like the presence of a clear preferential orientation along the (0 0 1) plane that occurs at 22.6° and a peak splitting around 59°, as previously described by Brayner *et al.* [29]. The low-intensity peaks of T-Nb_2O_5, such as the plane (1 3 0) at 17°, strongly suggest the TT and T crystalline phases mixture. The peak broadening and the preferential orientation along the (0 0 1) plane indicate that H3 has a higher amount of the TT-Nb_2O_5. Fig. 1(b) shows the Pair Distribution Function (PDF) analysis of these materials. The PDF analysis shows the first two bond values around 2.3 and 3.5 Å, corresponding to the first order coordination sphere bond between Nb-O and Nb-Nb, respectively. The H0, H1, and H2 samples did not present a long-range crystalline order, corroborating the XRD data. The signals between 4.3 and 12 Å indicate extended and most complex bonds between Nb and O atoms typical of the amorphous phase. The values of G(r) found for H3 show a long-range crystalline order up to 3 nm, which reinforces the crystalline features.

Figure S1 shows the N_2 physisorption analysis of the samples and the pore size distribution estimated by DFT method. Table 1 presents the textural properties of the samples obtained through the gas adsorption analysis. The H0, H1, and H2 samples presented a similar profile of a mixture of type I and IV isotherms [36,37]. Type I isotherms indicate

Table 1
Textural properties of the Nb_2O_5 materials from N_2 gas adsorption analysis.

Sample	SSA ($m^2\ g^{-1}$)	C*	Average Pore Diameter** (nm)	Total Pore Volume† ($cm^3\ g^{-1}$)	R^2
H0	165	450	3.4	0.215	0.999876
H1	126	72	26.9	1.19	0.999906
H2	90	71	3.8	0.182	0.999,891
H3	6	101	27.1	0.084	0.999,517

*Adjustment coefficient of the BET model.
**Measured employing DFT data from pore size distribution.
† Measured at the saturation point ($P/P^\circ = 0.99$).

microporous structure, which corroborates the adsorbed volume at low pressures. It shows a strong interaction between the photocatalyst and the N_2 molecules. Another feature observed is a sharp increase in the adsorbed volume at high pressures, which indicates the presence of a disordered macroporous structure. The type IV isotherms present a hysteresis loop and limit uptake at high pressures. These characteristics correlate with the mesoporous structure in the photocatalysts. However, no saturation regime was observed. These data show how much the textural properties of H0 change with the temperature of the calcination process [38].

The H0 sample is known for presenting micro and mesopores, with a strong interaction with N_2 [24]. It has a specific surface area (SSA) of 165 $m^2\ g^{-1}$ (Table 1), which is considered relatively high for niobium oxides. The H1 and H2 samples showed weaker adsorption at low pressures that could be explained by micropore closure of the system, with the H1 displaying very strong adsorption at high pressures. On the other hand, the closed hysteresis loop (around $P/P^\circ = 0.4$) indicates the formation of more organized mesopores in their structure. Heat treatment caused a decrease in SSA from 126 $m^2\ g^{-1}$ in H1 to 90 $m^2\ g^{-1}$ in H2 (temperature increased from 200 °C to 400 °C). This behavior was expected since pores collapse with increasing temperature, creating larger pores with weaker physical–chemical interaction with the adsorbed gas. The H3 sample has no significant SSA and showed a type III isotherm with negligible adsorption at intermediary pressures with a sharp increase at $P/P^\circ = 0.99$. The synthesis at 600 °C favored the crystallization of the T and TT phases, which caused the shrinking of SSA (6 $m^2\ g^{-1}$), total pore volume of 0.084 $cm^3\ g^{-1}$, and some residual mesopores.

The FTIR spectra (Figure S2 (a)) indicate that the synthesis temperature mainly affects the characteristic stretching bands of surface hydroxyls as well as adsorbed water (1617 and 3250 cm^{-1} [39]). The higher the temperature, the lower the intensity of these stretching; in the case of H3, these disappeared from the spectrum. Changes were also observed at lower wavenumbers values such as a decrease in signal intensity for the mode at 658 cm^{-1} while a new mode appeared at 793 cm^{-1} in the H3 sample. This phenomenon means that the temperature of 600 °C provided enough energy to form shorter bonds between Nb-O (more energetic stretches) [40], which is a direct indication of higher crystallization (in agreement with XRD data). The Kubelka-Munk functions obtained from the diffuse reflectance spectra, Figure S2 (b), showed that all synthesized Nb oxides absorb purely UV photons (<400 nm). As the radiation source applied in this study is in the UV-C region, centered at 254 nm, the slight band-gap difference does not limit photocatalysis.

3.2. Photocatalysis

Fig. 2(a) reveals that the conversion of LA increases proportionally with the annealing temperature of niobic acid. A sharp upgrade in the LA conversion from H0 to H1, 7.4% to 21.6% (difference of 14.2 %) was observed, that was the biggest difference at an increase of 200 °C in the entire series (i.e., H1-H0 > H2-H1 > H3-H2). The H3 reached the highest conversion, 36.4%, which shows that the increase in the synthesis temperature exerts a positive influence on LA photoreduction and photocatalysis do not seem to be sensitive to the decrease in the specific surface area, so it can be deduced that the depletion of hydroxyl groups as well as the generation of crystalline phases (at 600 °C) have a greater impact on the process. Another interesting fact was that this same photocatalyst, when submitted to the AET technique, unlike the others, changes the color from white to navy blue instead of dark gray (Figure S3). This optical phenomenon could be related to the TT-Nb_2O_5 crystalline phase.

The main LA-derived products generated during AET have already been described in our previous article [24]. Five main products were identified: ethyl levulinate (EL), γ-hydroxy valeric acid (GHV), γ-valerolactone (GVL), 6-hydroxy heptane 2,5-dione (HHD), and the γ-hydroxy ethyl valerate (GHE, or reduced ethyl levulinate) - see the molecular structures in Figure S4. The GHV result from the direct photocatalytic reduction of LA, while GVL is the intra-esterification product of GHV. EL can be produced via radical reactions and by esterification of LA with ethanol while GHE is generated by EL reduction, and the HHD is formed by the coupling of levulinyl and α-hydroxyethyl radicals [24].

The selectivity data for each product is shown in Fig. 2 (b). This value for the photoreduced compounds GVL, GHV, and GHE increases from H0 to H3. In contrast, from H1 to H3, EL was no longer detected, and HHD drastically decreased throughout the series. This result highlights that the thermal treatment of niobic acid favors the conversion of EL to GHE and avoids side reactions to form the HHD; in other words, it improves the AET process. This positive effect of temperature is reasonable since it reduces the hydroxyl concentration on the Nb_2O_5 surface (as shown in FTIR) and crystallizes its structure at 600 °C. It is well known that surface hydroxyls can trap photogenerated holes [15,41], so the decrease of these species favors the contact of holes with ethanol molecules, oxidizing them and consequently leading to the production of H^+ and e^- which are responsible for reducing levulinic acid, also the temperature crystallizes niobium oxide improving charge mobility and photon absorption [42,43]. No reduction products were detected in the absence of light or photocatalyst. In the case of the absence of UV radiation, both electrons and protons (generated as a product of ethanol oxidation) are not produced by the semiconductor, so LA cannot be reduced [24]. Without photocatalyst, UV light can only excite the π bond electrons of

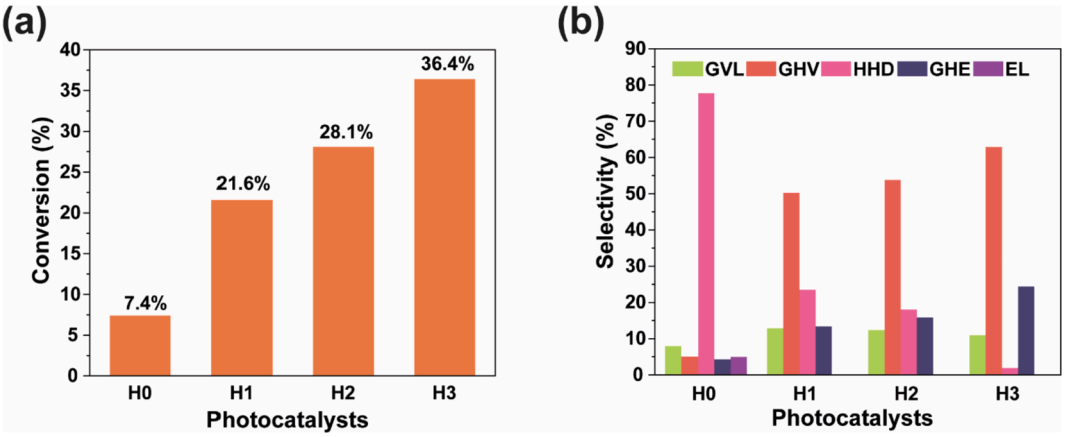

Fig. 2. **(a)** Conversion and **(b)** selectivity data for LA photoreduction, via AET, applying niobium oxides as photocatalysts. These data were obtained in 16 h of UV irradiation. The reaction conditions were: 0.2 mmol of LA, 2 mL of ethanol, 20 mg of photocatalyst, room temp, N_2 atmosphere and UV irradiation time of 16 h.

the carboxyl and carbonyl groups of levulinic acid, but these excited states in aliphatic systems have a very short lifetime and therefore no charge transfer occurs [44].

Reactions without the O_2 elimination step were done to evaluate the impact that the electron scavenger causes on the AET. The yield values of the photocatalytic reduction products are shown in Table 2. The yield increases approximately fivefold for H1, H2, and H3 in N_2 atmosphere. The yield for H0 in N_2 was slightly higher than in O_2 due to the reaction path (production of HHD mainly by the parallel reactions). Furthermore, molecular oxygen promotes ethanol oxidation to acetic acid, which is not observed in the N_2 atmosphere (it only oxidizes to acetaldehyde). Relatively high amounts of acetic acid were detected, reaching 0.47 mmol for H3.

A mechanism has been proposed to explain the formation of acetic acid from ethanol (Fig. 3). In the photocatalytic system containing O_2, two distinct processes occur simultaneously: the oxidation of ethanol to acetaldehyde by the holes in the valence band, Fig. 3(a), and the reduction of oxygen by electrons in the conduction band - Fig. 3(b). Molecular oxygen receives an electron, forming the superoxide radical, which is rapidly protonated (due to its pKa ~4.8 [15]), resulting in the hydroperoxyl radical. Hydroperoxyl is reduced to its anionic form, which attacks the carbonyl of acetaldehyde (Fig. 3(c), similar to acetalization process), and subsequently, a McLafferty-like rearrangement occurs, generating a neutral molecule (water) and acetate. Finally, the acetate is protonated to produce acetic acid.

H3 exhibited the highest photocatalytic activity for LA reduction via AET. Therefore, a new synthesis was developed in order to improve its photocatalytic activity. The new material was synthesized following the same heating parameters of H3, except by calcination in a 10 mL min^{-1} flow of 10% H_2 (90% N_2) gas mixture. The purpose of using hydrogen during the thermal treatment is to generate structural defects in niobium oxide, more specifically oxygen vacancies (OV), this is a well-known and used method to generate these species in oxides [45]. The OV make it possible to distinguish this photocatalyst, named H3OV, from others due to its grayish blue color (Figure S5) [46]. In addition to color, its DRS spectrum is quite distinct from that of H3 (Fig. 4(a)). Although its bandgap remains unchanged, a broad absorption band in the visible and near-infrared spectral ranges can be observed. Such defects induce internal states between the VB and CB (closer to CB than VB), allowing optical transitions in the mentioned spectral ranges. Another interesting fact is that these vacancies are quite stable, one month after H3OV synthesis a new spectrum was collected (not shown here) and no significant difference in DRS was observed. These OVs only revealed their paramagnetic nature below 30 K (due to their short relaxation time [29]), reaching the highest intensity at 10 K, where the spectra were recorded (Fig. 4(b)). A large signal with g = 2.00 was observed for H3OV. The broadening of this paramagnetic center may be related to the coupling of the vacancy electrons with the nuclear spin of ^{93}Nb (I = 9/2), resulting in 10 transition lines that an X-band spectrometer cannot resolve [19,20,29,47]. Furthermore, when the H3OV was subjected to *in situ* UV radiation, an additional gain of intensity (violet line plot) was observed, which indicates that more electrons were trapped in these defects. Meanwhile, under the same conditions, H3 did not show paramagnetic defects.

Table 2
Comparison of the yield of reduced products between the reaction with procedures for removing oxygen (N_2) and the reaction with atmospheric oxygen (O_2), for all photocatalysts. The reaction conditions were: 0.2 mmol of LA, 2 mL of ethanol, 20 mg of photocatalyst, room temp, N_2 or O_2 atmosphere and UV irradiation time of 16 h.

Photocatalyst	Yield (%)	
	N_2	O_2
H0	1.28	0.86
H1	16.54	3.18
H2	23.05	4.71
H3	35.68	6.97

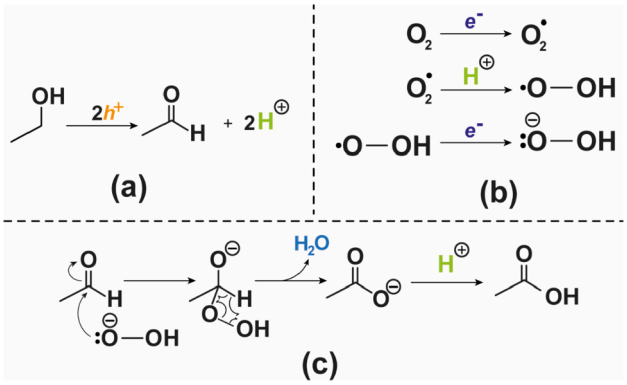

Fig. 3. Mechanistic proposal for the photocatalytic production of acetic acid. **(a)** Oxidation of ethanol to acetaldehyde, **(b)** reduction and protonation of oxygen to hydroperoxyl anion, and **(c)** reaction between acetaldehyde and hydroperoxyl anion to form acetate and consequently acetic acid.

To assess the structural behavior of H3 and H3OV, XRD experiments were carried out combined with Rietveld refinement analysis. Fig. 5(a) displays the XRD data of H3 and H3OV, which are very similar. However, the H3OV sample presented lower peak intensities and an apparent broadening than H3, typical from TT phase. Both materials have shown crystallization in TT and T modifications, but the characteristics of the H3OV indicate the majority presence of the TT phase. Fig. 5(b)–(e) shows the crystalline structure of the TT and T phases obtained through the Rietveld refinement of the H3 and H3OV XRD patterns, shown in Fig. 5(f) and (g). The opened structure (Fig. 5(b) and (d)) of the TT phase allows it to accommodate defects in its crystalline structure, differently from the T phase (Fig. 5(c) and (e)), which has higher atomic density. This structural engineering process is crucial to take advantage of the niobium pentoxide properties, which could be employed to produce defects (such as oxygen vacancies and edge dislocations) that enhance the photocatalytic performance [17,19,48].

Table 3 presents the Rietveld refinement results from the H3 and H3OV samples. The results showed reasonable confidence in the refinement analysis, showing small goodness of fit for all samples ($\chi^2 <$ 1.5), low Rp and Rwp values [49]. There are slight changes in the lattice parameters for the two samples due to differences in the bond lengths, angles, and microstrains values. The H3OV samples presented higher microstrain and dislocation density in both TT and T phases than H3, indicating that a reductive atmosphere (H_2) during the thermal treatment led to more defects in the crystalline structure. The crystallite size of H3OV presented smaller values than H3, which intrinsically correlates with the density dislocation values. Higher values mean that the samples have, statistically, more effects of peak enlargement due to broadening effects (microstrain and dislocation density) in the crystalline structure. The quantitative analysis obtained from Rietveld refinement indicates that H3OV samples showed a higher amount of TT-Nb_2O_5 than the H3, which corroborated higher microstrain and density dislocation values. This behavior occurs because the molecular hydrogen (H_2) creates a reductive environment during the thermal treatment process, creating more defects in the crystalline system, thus leading to the TT formation [50,51]. The N_2 adsorption isotherm and DFT pore distribution of H3OV displayed some differences from H3 (Figure S6). The H3OV has higher SSA (23 $m^2.g^{-1}$) and smaller pore size than H3. These features are due to the removal of oxygen from the lattice and the crystallinity transformations (higher content of the TT-modification) caused by the reducing atmosphere.

The differences between the H3 and H3OV samples were investigated employing the HRTEM technique. Fig. 6(a) and (b) show the TEM images for the H3 and H3OV, respectively. Both samples showed similar

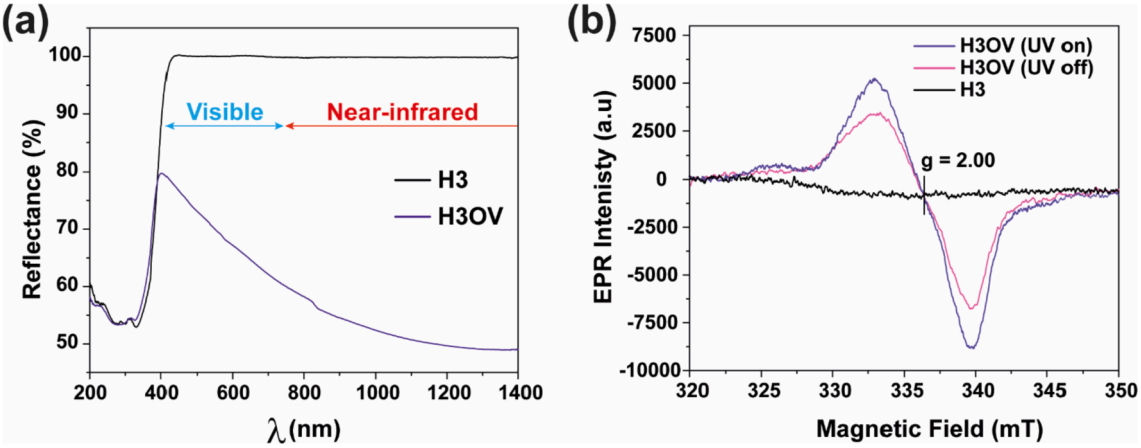

Fig. 4. **(a)** Difference between the diffuse reflectance spectra of H3 and H3OV **(b)** EPR powder spectra of H3 and H3OV measured at 10 K.

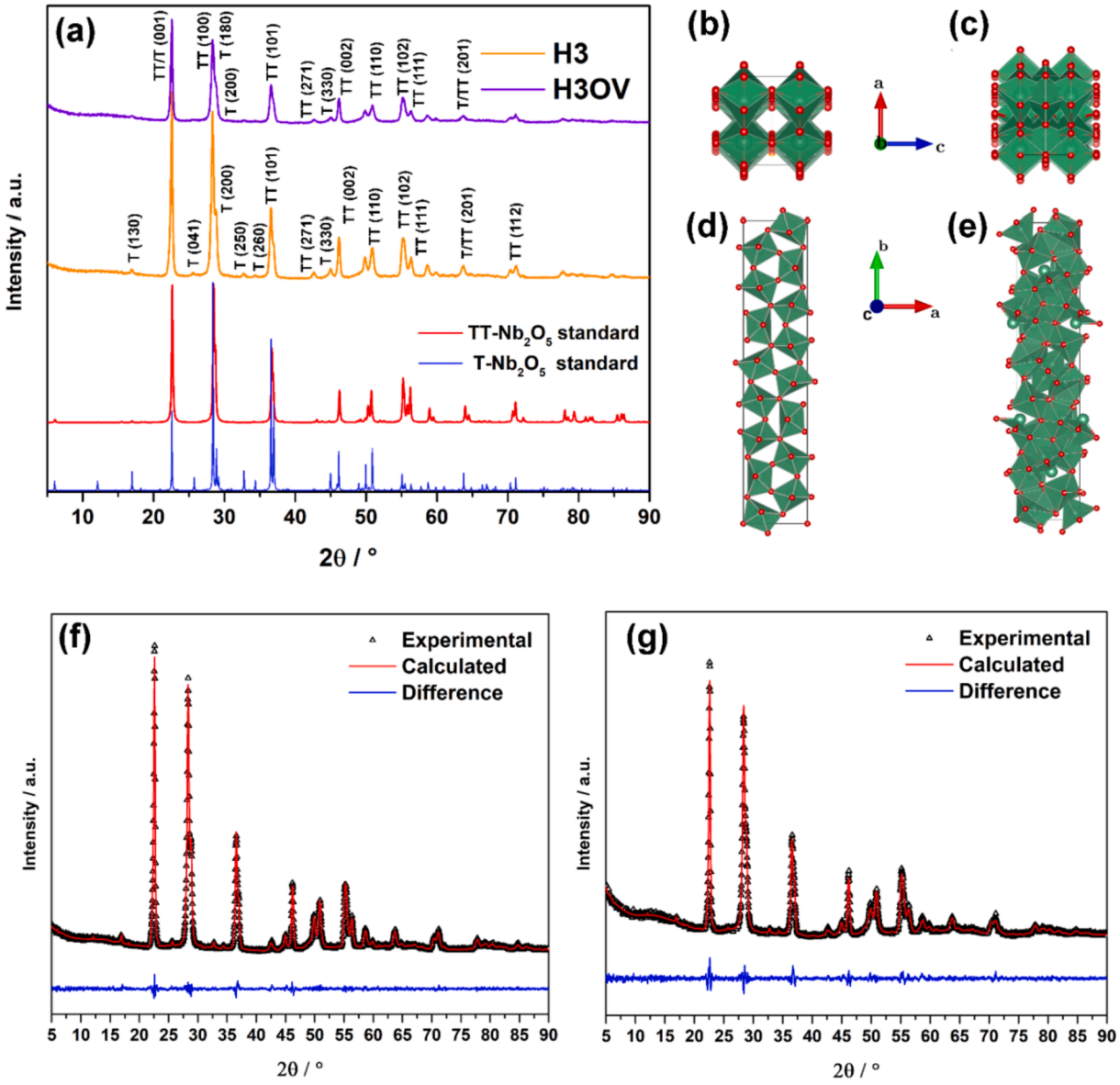

Fig. 5. **(a)** XRD patterns for H3 and H3OV samples, and the crystalline structures of **(b)** TT and **(c)** T phases along the b-axis, and **(d)** TT and **(e)** T phases along the c-axis. Rietveld refinement of **(f)** H3 and **(g)** H3OV.

Table 3
Rietveld refinement data from the H3 and H3OV samples.

Sample	Phase	Lattice Parameters/Å	Fraction/%	Crystallite Size/nm	Density dislocation/m⁻2	Strain/%	R_p/%	R_{wp}/%	χ^2
H3	TT- Nb_2O_5	a = 6.1836(1) b = 29.1102(7) c = 3.92080(2)	80.5	8	1.4×10^{16}	0.86	4.8	6.5	1.5
	T-Nb_2O_5	a = 6.1732(8) b = 29.235(8) c = 3.9248(8)	19.5	14	5.1×10^{15}	0.28			
H3OV	TT- Nb_2O_5	a = 6.1881(7) b = 29.077(6) c = 3.924(2)	90.4	7	1.9×10^{16}	0.94	5.46	7.2	1.3
	T- Nb_2O_5	a = 6.1706(0) b = 29.184(8) c = 3.9236(8)	9.6	11	8.0×10^{15}	0.45			

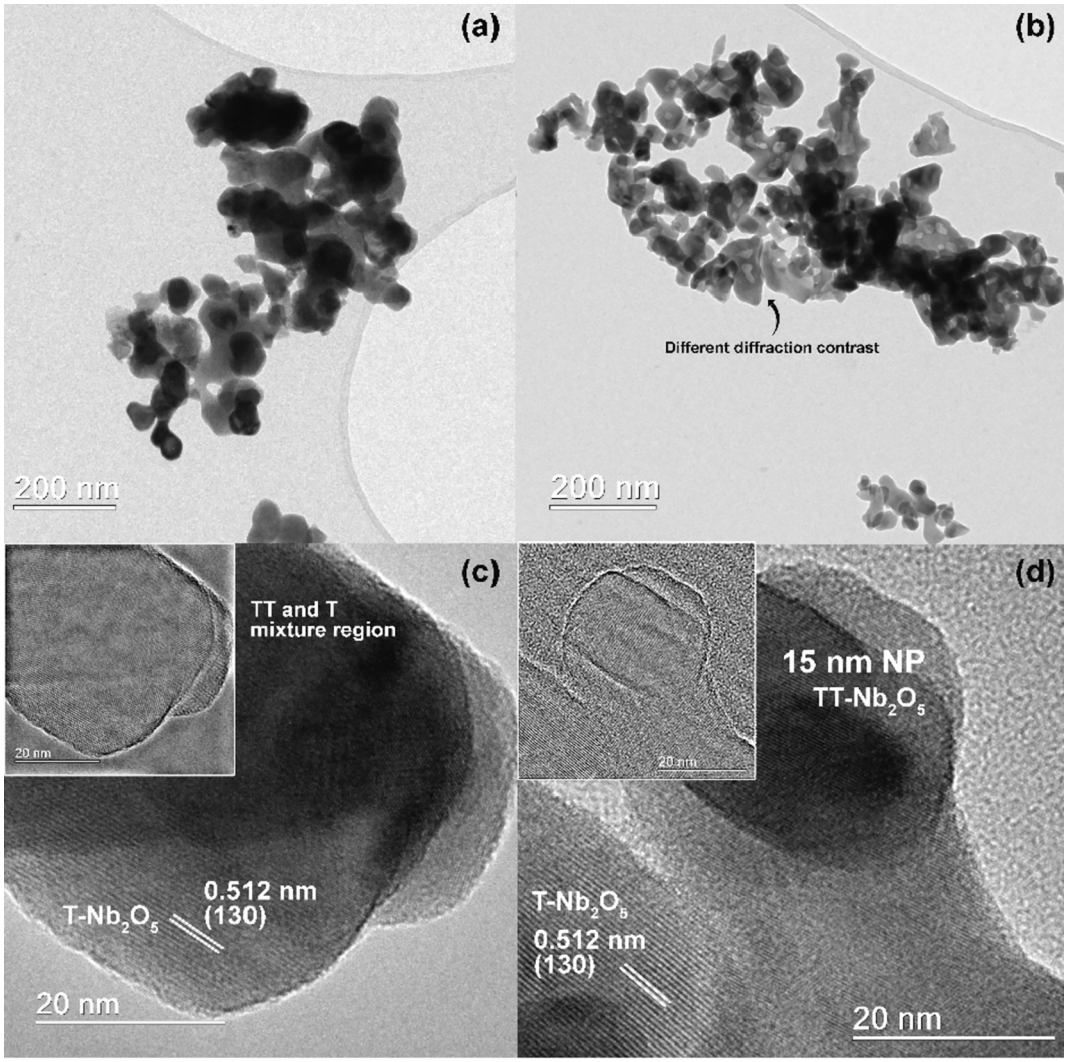

Fig. 6. TEM images of the **(a)** H3 and **(b)** H3OV. HRTEM images with inset Wiener filtering image for the **(c)** H3 and **(d)** H3OV samples.

morphology, with a clear agglomeration of round-shaped nanoparticles with different TEM contrasts. The H3OV presented smaller nanoparticles than H3 and brighter round-shaped spots inside darker and more prominent spots. Those characteristics are clear evidence of a phase mixture. The TT-Nb_2O_5 presents a smaller density value than T-Nb_2O_5 due to the open structure, in which the brighter and smaller spots are the TT-nanoparticles generated within the presence of T-nanoparticles. Fig. 6(c) and (d) show higher magnification and an inset Wiener filtering image of the H3 and H3OV nanoparticles, respectively. The H3OV presents smaller nanoparticles than H3, mainly due to a higher amount of TT-Nb_2O_5 crystalline phase in the samples, which corroborates the XRD and Rietveld refinement analysis. Fig. 6(c) and (d) show T-Nb_2O_5 with orientation on its exclusive (1 3 0) crystallographic plane, which made it easy to distinguish for the TT-nanoparticle. Another essential feature is the inhomogeneity of the diffraction contrast in the two samples. This phenomenon occurs due to an overlap of the crystallographic planes of TT and T-phases, which have quite similar crystalline structures with different packing densities. The

Wiener filter shows another perspective. The long-range crystalline order and the intergrowth of TT-nanoparticles in the structure are observable, leading to a disordered region with line defects, corroborating higher values of microstrain and dislocation density for the H3OV. For an in-depth discussion about the changes during T and TT phase transition see reference [30].

The Selected area electron diffraction (SAED) experiment was also carried out on the H3 and H3OV samples. These niobium oxides showed signals of the (1 0 1), (0 0 1), (1 0 0), (0 0 2) crystalline planes of the TT-modification. Fig. 7(a) and (b) show the SAED for the H3 and H3OV, respectively, pointing out the polycrystalline aspect. The signal intensity is weaker in the H3 analysis due to sample orientation and tilt. However, the two photocatalysts reveal less intense reflections filtering (Fig. 7(c) and (d)) and depicted the presence of a weak signal near the SAED (0 0 0) spot, which is attributed to the presence of (1 3 0) crystallographic plane of the T-phase. The filtering also provides more detailed information about the diffracted spots and indexes the planes seen in the image, highlighting the phase mixture. The (1 8 1) crystallographic plane occurs in the T-modification; however, they share a similar interplanar distance from the (1 0 1) plane from the TT-phase, making it difficult to distinguish both crystallographic planes in the SAED analysis.

Data from XPS measurements for Nb 3d and O 1 s energies are shown in Table 4 (these spectra are displayed in Figure S7). This analysis shows that H3 and H3OV have very similar surface properties. Both have Nb^{5+} [20,21,52] and the same oxygen species: lattice oxygens (O^{2-}), residual hydroxyls groups (OH), and electrodeficient lattice oxygens (O^{-}) [53,54]. A high concentration of O^{-} is observed on the surface of H3OV about H3. This species indirectly reflects the presence of vacancies in the structure of Nb_2O_5, since it is the counterpart that guarantees the electroneutrality of the solid. Another curious fact is that H3OV did not show any change in the binding energy of Nb 3d in comparison to H3, which suggests that OVs are not located on the surface. This result explains the stability of vacancies, as they are not located on the surface, atmospheric oxygen does not have access to these defects and therefore cannot oxidize them.

Table 4
XPS analysis parameters of H3 and H3OV.

Sample	H3	H3OV	Reference
	Binding Energy (eV)		
Nb^{5+} ($3d_{5/2}$)	206.30 ± 0.06	206.31 ± 0.09	207.5 ~ 206.9
Nb^{5+} ($3d_{3/2}$)	209.04 ± 0.05	209.03 ± 0.07	210.2 ~ 209.2
ΔE (Nb^{5+} 3d)	2.74	2.72	2.7
O 1 s (O^{2-})	529.29 ± 0.09	529.43 ± 0.04	530.5 ~ 527.7
O 1 s (OH^{-})	530.81 ± 0.02	530. 93 ± 0.07	530.5 ~ 531.0
O 1 s (O^{-})	531.5 ± 0.1	531.73 ± 0.06	531.0 ~ 532.0
	Atomic Weight (%)		
O^{2-}	91.73	85.00	–
OH^{-}	8.07	6.48	–
O^{-}	0.20	8.51	–

In order to evaluate the effect of the insertion of oxygen vacancies in the niobium oxide structure, H3OV was applied to the LA photocatalysis and compared to H3 (see Fig. 8). Although both semiconductors have a quite similar selectivity (Fig. 8(b)), H3OV had the best performance in LA conversion (Fig. 8(a), 7.1% increase compared to H3) and consequently in product yield. This makes H3OV the most active photocatalyst of the present study. No conversion was observed in the control test performed in the dark, which is reasonable since the vacancies are not on the surface. In addition, all photocatalytic results obtained in N_2 atmosphere of this study were also reported in $\mu mol.h^{-1}.g^{-1}$, please see Table S1 of the Supplementary Material. Typically, oxygen vacancies are associated with rapid charge recombination [55], the opposite of what was demonstrated by H3OV. Spin trapping kinetics were performed to

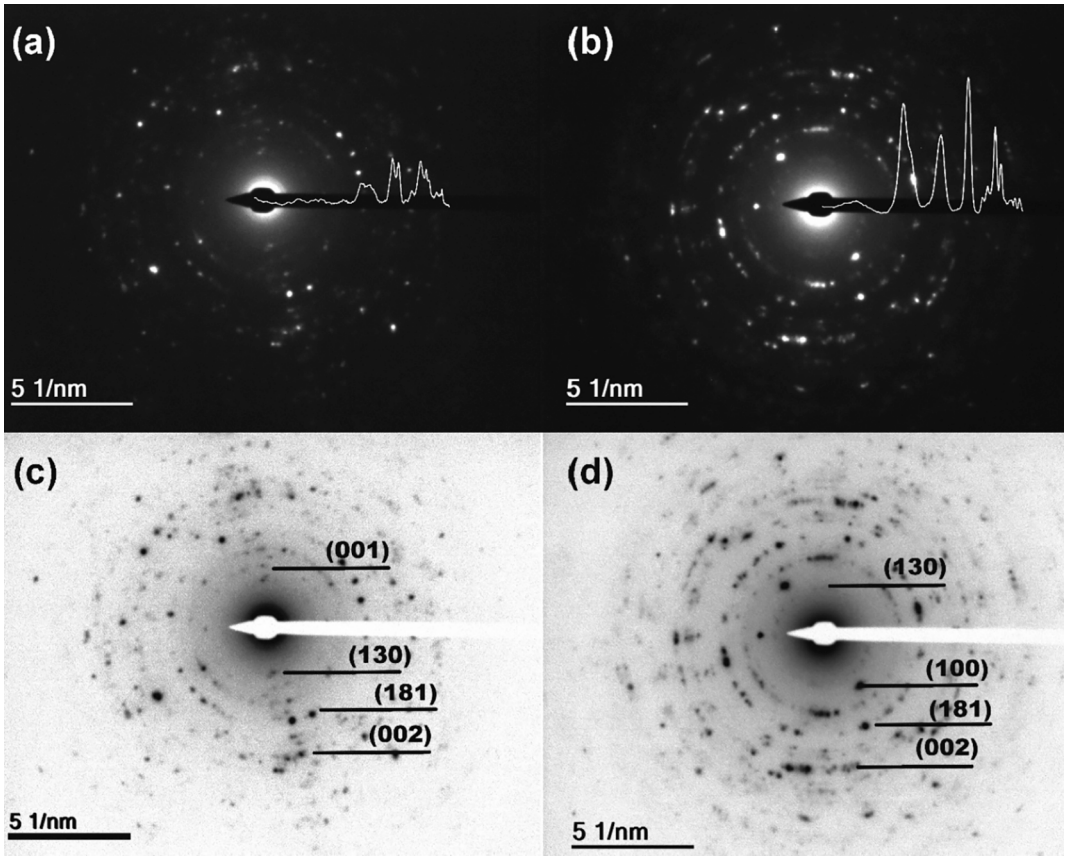

Fig. 7. SAED analysis of the **(a)** H3 and **(b)** H3OV with the interplanar distance signal inset, they reveal weak reflection filters for **(c)** H3 and **(d)** H3OV.

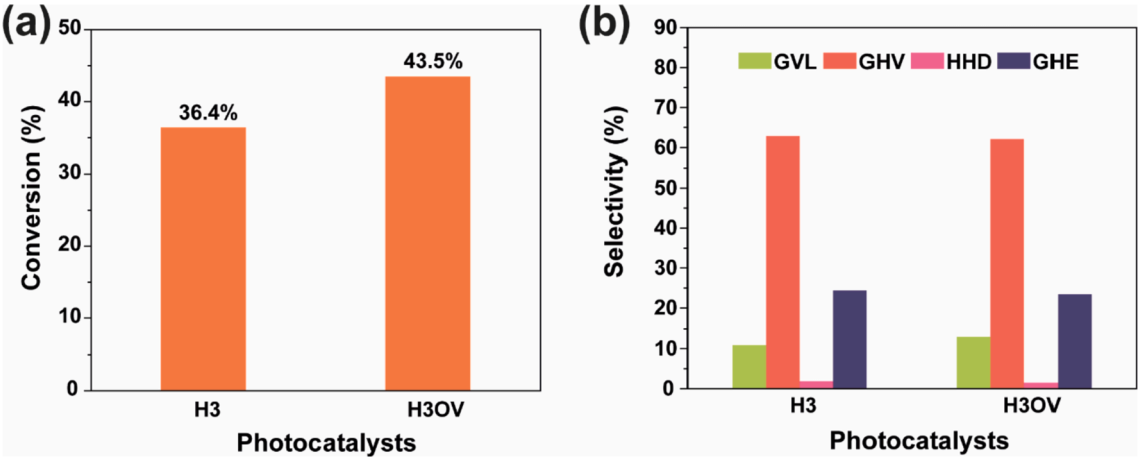

Fig. 8. Comparison between H3 and H3OV **(a)** conversion and **(b)** selectivities. The reaction conditions were: 0.2 mmol of LA, 2 mL of ethanol, 20 mg of photocatalyst, room temp, N_2 atmosphere and irradiation time of 16 h.

compare the charge recombination rate between H3 and H3OV by the difference in spin adduct generation. PBN was used to indirectly detect the holes generated in the VB (by trapping the ethanol radicals), while DMPO was applied to indirectly detect the electrons (by trapping the hydroperoxyl radical).

Interestingly, the hyperfine parameters of the PBN spin adduct found for both semiconductors (Fig. 9(a)) are characteristic of the ethoxy radical [56,57]. Previously, the majority of α-hydroxy ethyl production was reported for H0 [24]. Perhaps the changes caused on the surface by the thermal treatment (loss of hydroxyls shown by FTIR) may have modified the nature in which ethanol interacts and, consequently, the radical production. Furthermore, the ethoxy radical explains the selectivity for GHE shown by H3 and H3OV, whereas H0 basically produces HHD. The sextet EPR spectrum of the DMPO spin adduct indicated that both niobium oxides produced the hydroperoxyl radical (Fig. 9(c)), the low-intensity triplet deconvoluted by the simulation is associated with the degradation of this spin trap. Looking at the kinetic curves of ethoxy and hydroperoxyl radical evolution (Fig. 9(b) and (d)), there is practically no difference between H3 and H3OV, i.e., the OVs, in this case, do not behave as recombination centers. As the presence of these defects

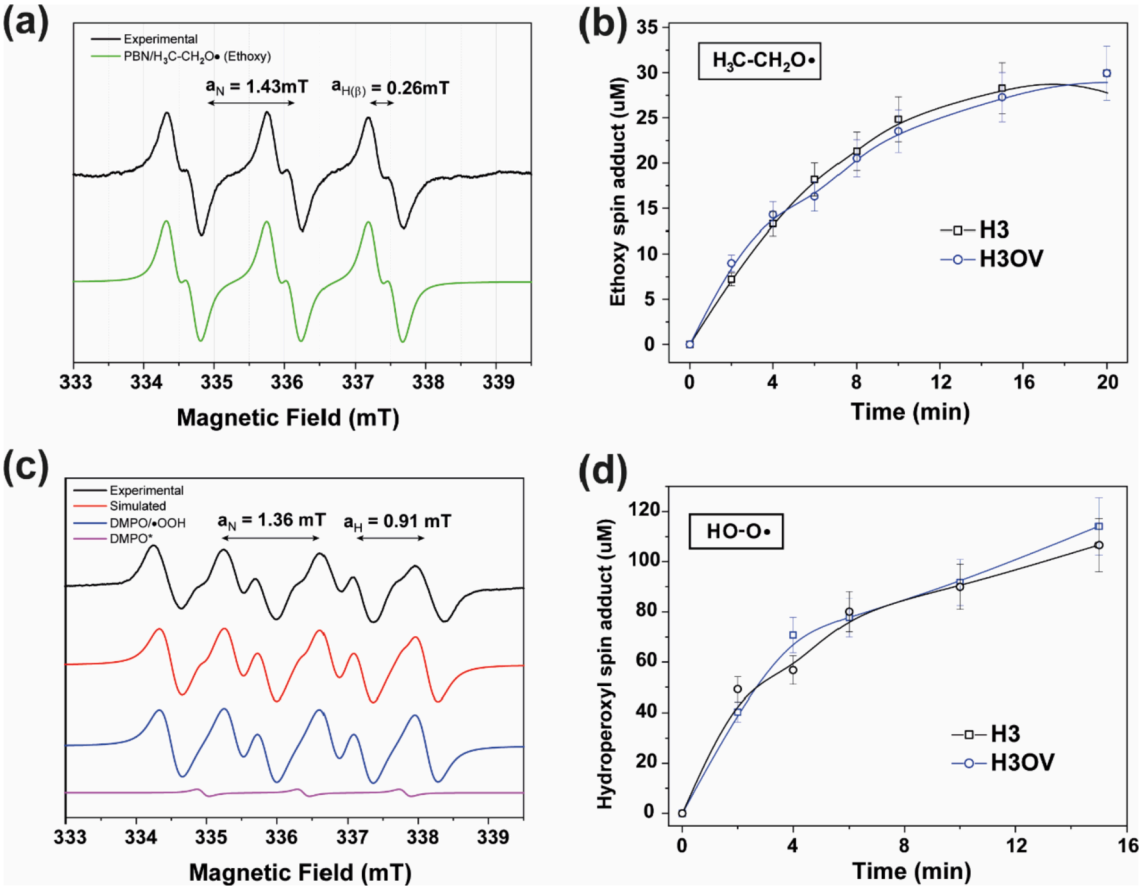

Fig. 9. (a) Experimental and simulated spectra of spin trapping measurements with PBN, **(b)** kinetic curves of the PBN spin adducts for H3 and H3OV, **(c)** Experimental and simulated spectra of the spin trapping measurements with DMPO and **(d)** kinetic curves of the spin adducts of the PBN for H3 and H3OV.

was not detected by XPS, these vacancies may be in the subsurface of the material. Literature studies suggest that OVs are deleterious to photocatalytic performance if they are in the bulk; subsurface and surface vacancies favor the reactions [58–60]. On top of that, EPR powder measurements have shown an increase of electron density in OVs when H3OV is illuminated, possibly such an electron trapping could be involved in reducing the rate of charge recombination as well as increasing the number of electrons available to reduce LA.

As H3OV presented visible light absorption, a reaction was performed using a white LED lamp (Stella, 5 $mW.cm^{-2}$ of luminous power, emission spectrum already characterized [52]) to verify any photocatalytic activity in this spectral range for LA conversion. It is essential for a possible application under solar energy. Unlike UV photocatalysis, the visible reaction resulted in a much lower conversion, which was already expected from the source energy, 4.1% versus 43.5% for UV and a different selectivity (Fig. 10(a) and (b)). In UV photocatalysis, the highest selectivity value was obtained for GHV. Under visible light irradiation, this position was occupied by HHD. As noted in the previous work, HHD is generated by side radical reactions between levulinic acid and ethanol but at longer reaction times, it turns to GVL [24]. Despite the poor conversion value of LA as well as low selectivity for reduction products, compared to UV radiation, H3OV is still able to generate GVL, GHV, and GHE in the visible, which is an outstanding result.

To confirm whether such material can generate photogenerated charges in the visible, spin trapping tests (DMPO and PBN) were also carried out with this type of radiation. The identical spin adducts detected in UV were observed in 10 min of visible radiation (Figures S8 (a) and (b)), with much lower intensity nevertheless (the noise is evident in the experimental curves). These experiments prove that the H3OV can separate the e^-/h^+ pairs under visible light. Contradictory to the results of photocatalysis, the radical observed for the visible radiation was the ethoxy. The HHD product is produced by C–C coupling between levulinyl radical with α-hydroxy ethyl radical and not with ethoxy [24].

Visible light cannot excite the electron directly from VB to CB, only from VB to OV and/or from OV to CB, this last transition is less energetic, responsible for the absorption of NIR by the material (see the Density of States diagram, Fig. 10(c)) [58,60,61]. This "transition shortcut" does not effectively transfer the electron to the LA, so these electrons promote the reverse path of the scavenger (ethanol), reducing the acetaldehyde to α-hydroxy ethyl. Then it reacts with the levulinyl species. In this process, ethoxy is a kinetic radical, while α-hydroxy ethyl is thermodynamic. From the organic chemistry point of view, radicals are compounds favored mainly by resonance. Among these two produced from ethanol, only α-hydroxy ethyl can make resonance (the entire process is in Fig. 10(d)), making it more thermodynamically stable. Therefore it is preferably generated in the reduction of acetaldehyde.

4. Conclusions

Niobium oxides H1, H2, and H3 were synthesized from H0 via thermal treatment (200 °C, 400 °C, and 600 °C, respectively). Among them, H3 proved to be the best photocatalyst for reducing LA, reaching 36.4% of conversion and almost 99% of selectivity for reduced products. This niobium oxide lost all the surface hydroxyls groups and showed no micro and mesoporosity due to the formation of T and TT phase crystallites, such a result means that for LA photoreduction, the lack of hydroxyls and crystalline phases are crucial properties. Tests in the ambient air atmosphere (instead of N_2) showed the deleterious effect of O_2 as electron scavenger. For H3, the yield of reduction products dropped about five times when molecular oxygen was present. The

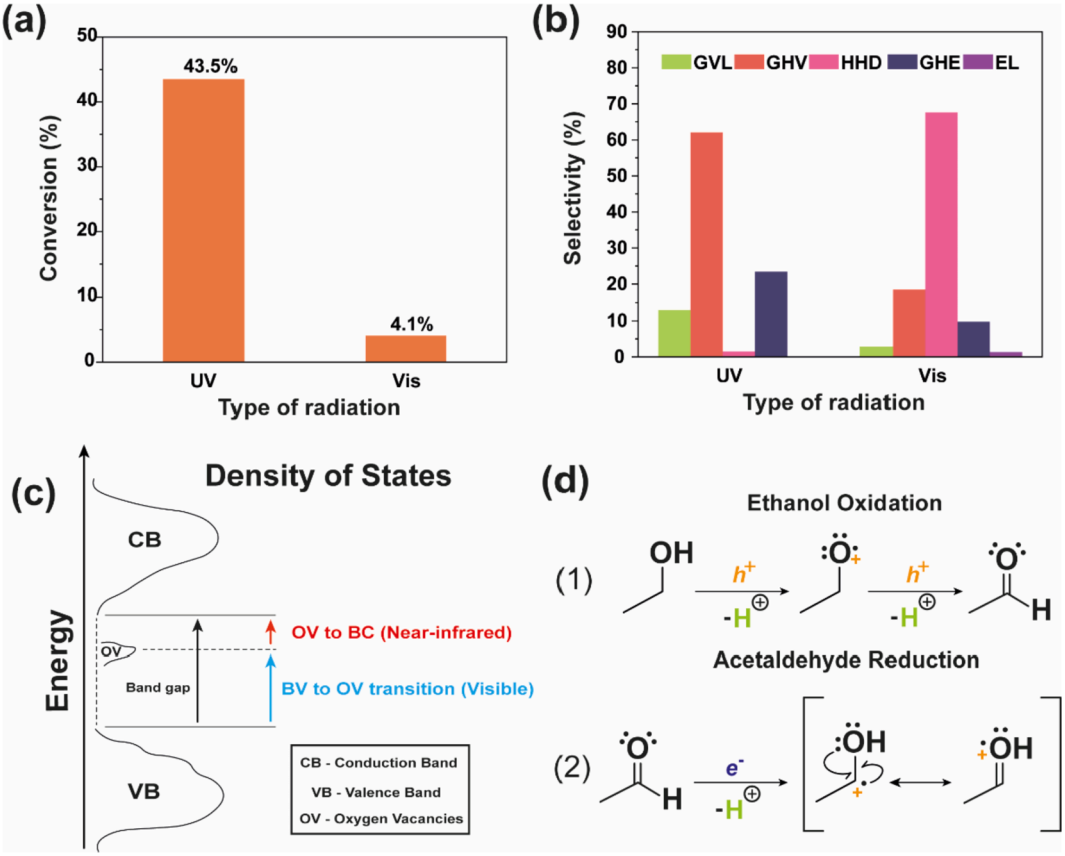

Fig. 10. **(a)** Comparison of the conversion, **(b)** selectivity data between UV and Visible photocatalysis for H3OV, the reaction conditions were: 0.2 mmol of LA, 2 mL of ethanol, 20 mg of photocatalyst, room temp, N_2 atmosphere and irradiation time of 16 h; **(c)** Density of State illustrative diagram for H3OV and **(d)** oxidation of ethanol to acetaldehyde (1) and the formation of α-hydroxy ethyl from acetaldehyde (2).

oxygen vacancies generated during H3OV synthesis improved 7.1% of LA reduced products yield. These stable oxygen vacancies were detected by DRS and EPR, also Rietveld's refinement of H3OV showed a higher fraction of TT-phase than H3. The XPS analysis showed that the oxygen vacancies are not on the subsurface of H3OV, which explains their stability. H3OV also showed photocatalytic activity in the visible spectral range. It is ten times lower than UV, however the selectivity was quite different: the HHD was generated as the main product in the visible light, while GHV in UV photocatalysis. This fact indicates that the mechanism in visible spectral range proceeds differently, most of the accumulated electrons reduce back the acetaldehyde to the α-hydroxyethyl radical (this species is thermodynamically more favorable), that couples with the levulinyl radical producing HHD. All these results proved that it is possible to significantly increase the photocatalytic performance of the semiconductor without laborious modifications or adding cocatalysts.

Declaration of Competing Interest

The authors declare that they have no known competing financial interests or personal relationships that could have appeared to influence the work reported in this paper.

Data availability

No data was used for the research described in the article.

Acknowledgments

This study was only possible thanks to the funding agencies Capes, CNPq and Fapemig. Also, the authors are grateful to the UFMG Microscopy Center for assisting the research with its excellent infrastructure and to CBMM for providing the HY-340 for free.

Appendix A. Supplementary data

Supplementary data to this article can be found online at https://doi.org/10.1016/j.cej.2022.137935.

References

[1] J.J. Bozell, G.R. Petersen, Technology development for the production of biobased products from biorefinery carbohydrates - The US Department of Energy's "top 10" revisited, Green Chem. 12 (2010) 539–554, https://doi.org/10.1039/b922014c.
[2] T. Werpy, G. Petersen, Top Value Added Chemicals from Biomass Volume I, Us Nrel. (2004) Medium: ED; Size: 76 pp. pages. https://doi.org/10.2172/15008859.
[3] H.P. Winoto, Z.A. Fikri, J.M. Ha, Y.K. Park, H. Lee, D.J. Suh, J. Jae, Heteropolyacid supported on Zr-Beta zeolite as an active catalyst for one-pot transformation of furfural to Γ-valerolactone, Appl. Catal. B Environ. 241 (2019) 588–597, https://doi.org/10.1016/j.apcatb.2018.09.031.
[4] X. Huang, K. Liu, W.L. Vrijburg, X. Ouyang, A. Iulian Dugulan, Y. Liu, M.W.G. M. Tiny Verhoeven, N.A. Kosinov, E.A. Pidko, E.J.M. Hensen, Hydrogenation of levulinic acid to γ-valerolactone over Fe-Re/TiO_2 catalysts, Appl. Catal. B Environ. 278 (2020) 119314, https://doi.org/10.1016/j.apcatb.2020.119314.
[5] D.R. Chaffey, T. Bere, T.E. Davies, D.C. Apperley, S.H. Taylor, A.E. Graham, Conversion of levulinic acid to levulinate ester biofuels by heterogeneous catalysts in the presence of acetals and ketals, Appl. Catal. B Environ. 293 (2021), 120219, https://doi.org/10.1016/j.apcatb.2021.120219.
[6] C. Gao, J. Low, R. Long, T. Kong, J. Zhu, Y. Xiong, Heterogeneous single-atom photocatalysts: fundamentals and applications, Chem. Rev. 120 (2020) 12175–12216, https://doi.org/10.1021/acs.chemrev.9b00840.
[7] V. Navakoteswara Rao, T.J. Malu, K.K. Cheralathan, M. Sakar, S. Pitchaimuthu, V. Rodríguez-González, M. Mamatha Kumari, M.V. Shankar, Light-driven transformation of biomass into chemicals using photocatalysts – Vistas and challenges, J. Environ. Manage. 284 (2021) 111983, https://doi.org/10.1016/j.jenvman.2021.11983.
[8] H. Zhao, C.F. Li, X. Yu, N. Zhong, Z.Y. Hu, Y. Li, S. Larter, M.G. Kibria, J. Hu, Mechanistic understanding of cellulose β-1,4-glycosidic cleavage via photocatalysis, Appl. Catal. B Environ. 302 (2022) 1–8, https://doi.org/10.1016/j.apcatb.2021.120872.
[9] H. Zhang, M. Zhao, T. Zhao, L. Li, Z. Zhu, Hydrogenative cyclization of levulinic acid into γ-valerolactone by photocatalytic intermolecular hydrogen transfer, Green Chem. 18 (2016) 2296–2301, https://doi.org/10.1039/c5gc02971f.
[10] U. Nwosu, A. Wang, B. Palma, H. Zhao, M.A. Khan, M. Kibria, J. Hu, Selective biomass photoreforming for valuable chemicals and fuels: a critical review, Renew. Sustain. Energy Rev. 148 (2021), 111266, https://doi.org/10.1016/j.rser.2021.111266.
[11] D. Friedmann, A. Hakki, H. Kim, W. Choi, D. Bahnemann, Heterogeneous photocatalytic organic synthesis: state-of-the-art and future perspectives, Green Chem. 18 (2016) 5391–5411, https://doi.org/10.1039/c6gc01582d.
[12] R. Qian, H. Zong, J. Schneider, G. Zhou, T. Zhao, Y. Li, J. Yang, D.W. Bahnemann, J.H. Pan, Charge carrier trapping, recombination and transfer during TiO_2 photocatalysis: an overview, Catal. Today. 335 (2019) 78–90, https://doi.org/10.1016/j.cattod.2018.10.053.
[13] L.I. Granone, F. Sieland, N. Zheng, R. Dillert, D.W. Bahnemann, Photocatalytic conversion of biomass into valuable products: a meaningful approach? Green Chem. 20 (6) (2018) 1169–1192.
[14] M. Liu, T. Peng, H. Li, L. Zhao, Y. Sang, Q. Feng, L. Xu, Y. Jiang, H. Liu, J. Zhang, Photoresponsive nanostructure assisted green synthesis of organics and polymers, Appl. Catal. B Environ. 249 (2019) 172–210, https://doi.org/10.1016/j.apcatb.2019.02.071.
[15] Y. Nosaka, A.Y. Nosaka, Generation and detection of reactive oxygen species in photocatalysis, Chem. Rev. 117 (2017) 11302–11336, https://doi.org/10.1021/acs.chemrev.7b00161.
[16] S. Kohtani, E. Yoshioka, K. Saito, A. Kudo, H. Miyabe, Photocatalytic hydrogenation of acetophenone derivatives and diaryl ketones on polycrystalline titanium dioxide, Catal. Commun. 11 (2010) 1049–1053, https://doi.org/10.1016/j.catcom.2010.04.022.
[17] O. Al-Madanat, B.N. Nunes, Y. AlSalka, A. Hakki, M. Curti, A.O.T. Patrocinio, D. Bahnemann, Application of EPR spectroscopy in TiO_2 and Nb_2O_5 photocatalysis, Catalysts 11 (2021) 1514.
[18] Y. Wang, X. Hu, H. Song, Y. Cai, Z. Li, D. Zu, P. Zhang, D. Chong, N. Gao, Y. Shen, C. Li, Oxygen vacancies in actiniae-like Nb_2O_5/Nb_2C MXene heterojunction boosting visible light photocatalytic NO removal, Appl. Catal. B Environ. 299 (2021), 120677, https://doi.org/10.1016/j.apcatb.2021.120677.
[19] K. Su, H. Liu, Z. Gao, P. Fornasiero, F. Wang, Nb_2O_5-based photocatalysts, Adv. Sci. 8 (2021) 1–25, https://doi.org/10.1002/advs.202003156.
[20] T. Song, C. Wang, Y. Zhang, X. Shi, Y. Li, Y. Yang, Visible-light-induced oxidative alkene difunctionalization to access α-sulfonyloxy ketones catalyzed by oxygen-vacancy-rich Nb_2O_5, Appl. Catal. B Environ. 304 (2022) 120964, https://doi.org/10.1016/j.apcatb.2021.120964.
[21] A.M. Mokhtar, K.E. Salem, N.K. Allam, Multiple synergistic effects of Zr-alloying on the phase stability and photostability of black niobium oxide nanotubes as efficient photoelectrodes for solar hydrogen production, Appl. Catal. B Environ. 287 (2021), 119961, https://doi.org/10.1016/j.apcatb.2021.119961.
[22] X. Ma, X. Li, J. Zhou, Y. Wang, X. Lang, Anchoring dye onto 1D Nb_2O_5 in cooperation with TEMPO for the selective photocatalytic aerobic oxidation of amines, Chem. Eng. J. 426 (2021), 131418, https://doi.org/10.1016/j.cej.2021.131418.
[23] C. Peng, X. Xie, W. Xu, T. Zhou, P. Wei, J. Jia, K. Zhang, Y. Cao, H. Wang, F. Peng, R. Yang, X. Yan, H. Pan, H. Yu, Engineering highly active Ag/Nb_2O_5@Nb_2CTx (MXene) photocatalysts via steering charge kinetics strategy, Chem. Eng. J. 421 (2021), 128766, https://doi.org/10.1016/j.cej.2021.128766.
[24] J.B.G. Filho, R.D.F. Rios, C.G.O. Bruziquesi, D.C. Ferreira, H.F.V. Victória, K. Krambrock, M.C. Pereira, L.C.A. Oliveira, A promising approach to transform levulinic acid into γ-valerolactone using niobic acid photocatalyst and the accumulated electron transfer technique, Appl. Catal. B Environ. 285 (2021) 119814, https://doi.org/10.1016/j.apcatb.2020.119814.
[25] C.L. Farrow, P. Juhas, J.W. Liu, D. Bryndin, E.S. Božin, J. Bloch, T. Proffen, S.J. L. Billinge, PDFfit2 and PDFgui : computer programs for studying nanostructure in crystals, J. Phys. Condens. Matter. 19 (2007) 1–7, https://doi.org/10.1088/0953-8984/19/33/335219.
[26] P. Juhás, T. Davis, C.L. Farrow, S.J.L. Billinge, PDFgetX3: a rapid and highly automatable program for processing powder diffraction data into total scattering pair distribution functions, Appl. Crystallogr. 46 (2013) 560–566, https://doi.org/10.1107/S0021889813005190.
[27] V. I. Korsunskiy, R.B. Neder, A. Hofmann, S. Dembski, C. Graf, E. Rühl, Aspects of the modelling of the radial distribution function for small nanoparticles, J Appl Crystallogr 40 (6) (2007) 975–985.
[28] S. Stoll, A. Schweiger, EasySpin, a comprehensive software package for spectral simulation and analysis in EPR, J. Magn. Reson. 178 (2006) 42–55, https://doi.org/10.1016/j.jmr.2005.08.013.
[29] R. Brayner, F. Bozon-Verduraz, Niobium pentoxide prepared by soft chemical routes: morphology, structure, defects and quantum size effect, Phys. Chem. Chem. Phys. 5 (2003) 1457–1466, https://doi.org/10.1039/b210055j.
[30] G.H.d.M. Gomes, R.R.d. Andrade, N.D.S. Mohallem, Investigation of phase transition employing strain mapping in TT- and T-Nb_2O_5 obtained by HRTEM micrographs, Micron. 148 (2021) 103112, https://doi.org/10.1016/j.micron.2021.103112.
[31] G.H.M. Gomes, N.D.S. Mohallem, CCDC 2103847: experimental crystal structure determination, ICSD Commun. (2021). https://doi.org/10.25505/fiz.icsd.cc28m716.
[32] K. Kato, S. Tamura, Die kristallstruktur von T-Nb_2O_5, Acta Crystallogr. Sect. B Struct. Crystallogr. Cryst. Chem. 31 (1975) 673–677, https://doi.org/10.1107/s0567740875003603.
[33] H. Schäfer, R. Gruehn, F. Schulte, The modifications of niobium pentoxide, Angew. Chemie Int. Ed. English. 5 (1966) 40–52, https://doi.org/10.1002/anie.196600401.

[34] J.G. Weissman, E.I. Ko, P. Wynblatt, J.M. Howe, High-resolution electron microscopy and image simulation of TT-, T-, and H-Niobia and model silica supported niobium surface oxides, Chem. Mater. 1 (2) (1989) 187–193.
[35] G.H.M. Gomes, N.D.S. Mohallem, Insights into the TT-Nb_2O_5 crystal structure behavior, Mater. Lett. 318 (2022), 132136, https://doi.org/10.1016/j.matlet.2022.132136.
[36] K.S.W. Sing, INTERNATIONALUNION OF PUREAND APPLIED CHEMISTRY, Pure Appl. Chem. 54 (1982) 2201–2218.
[37] M. Thommes, K. Kaneko, A.V. Neimark, J.P. Olivier, F. Rodriguez-reinoso, J. Rouquerol, K.S.W. Sing, Physisorption of gases, with special reference to the evaluation of surface area and pore size distribution (IUPAC Technical Report), Pure Appl. Chem. 87 (2015) 1051–1069, https://doi.org/10.1515/pac-2014-1117.
[38] K.S.W. Sing, The use of gas adsorption for the characterization of porous solids, Colloids Surfaces 38 (1989) 113–124, https://doi.org/10.1016/0166-6622(89)80148-9.
[39] A. Esteves, L.C.A. Oliveira, T.C. Ramalho, M. Goncalves, A.S. Anastacio, H.W. P. Carvalho, New materials based on modified synthetic Nb_2O_5 as photocatalyst for oxidation of organic contaminants, Catal. Commun. 10 (2008) 330–332, https://doi.org/10.1016/j.catcom.2008.09.012.
[40] H.T. Kreissl, M.M.J. Li, Y.K. Peng, K. Nakagawa, T.J.N. Hooper, J.V. Hanna, A. Shepherd, T.S. Wu, Y.L. Soo, S.C.E. Tsang, Structural studies of bulk to nanosize niobium oxides with correlation to their acidity, J. Am. Chem. Soc. 139 (2017) 12670–12680, https://doi.org/10.1021/jacs.7b06856.
[41] R.F. Howe, M. Grätzel, EPR study of hydrated anatase under UV irradiation, J. Phys. Chem. 91 (1987) 3906–3909, https://doi.org/10.1021/j100298a035.
[42] N.T. do Prado, L.C.A. Oliveira, Nanostructured niobium oxide synthetized by a new route using hydrothermal treatment: high efficiency in oxidation reactions, Appl. Catal. B Environ. 205 (2017) 481–488, https://doi.org/10.1016/j.apcatb.2016.12.067.
[43] F. Parrino, M. Bellardita, E.I. García-López, G. Marcì, V. Loddo, L. Palmisano, Heterogeneous photocatalysis for selective formation of high-value-added molecules: some chemical and engineering aspects, ACS Catal. 8 (2018) 11191–11225, https://doi.org/10.1021/acscatal.8b03093.
[44] T.Y. Shang, L.H. Lu, Z. Cao, Y. Liu, W.M. He, B. Yu, Recent advances of 1,2,3,5-tetrakis(carbazol-9-yl)-4,6-dicyanobenzene (4CzIPN) in photocatalytic transformations, Chem. Commun. 55 (2019) 5408–5419, https://doi.org/10.1039/c9cc01047e.
[45] R. Jain, A. Dubey, M.K. Ghosalya, C.S. Gopinath, Gas-solid interaction of H2-$Ce_{0.95}Zr_{0.05}O_2$: new insights into surface participation in heterogeneous catalysis, Catal. Sci. Technol. 6 (2016) 1746–1756, https://doi.org/10.1039/c5cy01428j.
[46] A.S. Burange, R. Shukla, A.K. Tyagi, C.S. Gopinath, Palladium supported on fluorite structured redox $CeZrO_4$-δ for heterogeneous suzuki coupling in water: a green protocol, ChemistrySelect 1 (2016) 2673–2681, https://doi.org/10.1002/slct.201600655.
[47] Y. Zou, Y. Hu, A. Uhrich, Z. Shen, B. Peng, Z. Ji, M. Muhler, G. Zhao, X. Wang, X. Xu, Steering accessible oxygen vacancies for alcohol oxidation over defective Nb_2O_5 under visible light illumination, Appl. Catal. B Environ. 298 (2021), 120584, https://doi.org/10.1016/j.apcatb.2021.120584.
[48] H.L. Tuller, S.R. Bishop, Point defects in oxides: tailoring materials through defect engineering, Annu. Rev. Mater. Res. 41 (2011) 369–398, https://doi.org/10.1146/annurev-matsci-062910-100442.
[49] B.H. Toby, R factors in rietveld analysis: how good is good enough? Powder Diffr. 21 (2006) 67–70, https://doi.org/10.1154/1.2179804.
[50] T. Sreethawong, S. Ngamsinlapasathian, S.H. Lim, S. Yoshikawa, Investigation of thermal treatment effect on physicochemical and photocatalytic H_2 production properties of mesoporous-assembled Nb_2O_5 nanoparticles synthesized via a surfactant-modified sol-gel method, Chem. Eng. J. 215–216 (2013) 322–330, https://doi.org/10.1016/j.cej.2012.11.023.
[51] T.L. Valerio, G. Tractz, G.A. Rodrigues Maia, E.d.P. Banczek, P.R. Pinto Rodrigues, Minimizing of charge recombination by Nb_2O_5 addition in dye-sensitized solar cells, Opt. Mater. (Amst). 109 (2020) 110310.
[52] J.B.G. Filho, C.G.O. Bruziquesi, R.D.F. Rios, A.A. Castro, H.F.V. Victória, K. Krambrock, A.A.P. Mansur, H.S. Mansur, R.D. Siniterra, T.C. Ramalho, M. C. Pereira, L.C.A. Oliveira, Selective visible-light-driven toxicity breakdown of nerve agent simulant methyl paraoxon over a photoactive nanofabric, Appl. Catal. B Environ. 285 (2021) 119774, https://doi.org/10.1016/j.apcatb.2020.119774.
[53] N.A. Merino, B.P. Barbero, P. Eloy, L.E. Cadús, La_1-xCaxCoO_3 perovskite-type oxides: identification of the surface oxygen species by XPS, Appl. Surf. Sci. 253 (2006) 1489–1493, https://doi.org/10.1016/j.apsusc.2006.02.035.
[54] J.C. Dupin, D. Gonbeau, P. Vinatier, A. Levasseur, Systematic XPS studies of metal oxides, hydroxides and peroxides, Phys. Chem. Chem. Phys. 2 (2000) 1319–1324, https://doi.org/10.1039/a908800h.
[55] M. Janczarek, E. Kowalska, Defective dopant-free TiO_2 as an efficient visible light-active photocatalyst, Catalysts 11 (8) (2021) 978.
[56] G.R. Buettner, SPIN TRAPPING: ESR PARAMETERS OF SPIN ADDUCTS, Free Radic. Biol. Med. 3 (1987) 259–303, https://doi.org/10.1016/s0891-5849(87)80033-3.
[57] C.A. Jenkins, D.M. Murphy, C.C. Rowlands, T.A. Egerton, EPR study of spin-trapped free radical intermediates formed in the heterogeneously-assisted photodecomposition of acetaldehyde, J. Chem. Soc. Perkin Trans. 2 (1997) 2479–2486, https://doi.org/10.1039/a702944f.
[58] L. Hao, H. Huang, Y. Zhang, T. Ma, Oxygen vacant semiconductor photocatalysts, Adv. Funct. Mater. 31 (2021) 1–32, https://doi.org/10.1002/adfm.202100919.
[59] J. Cai, A. Cao, J. Huang, W. Jin, J. Zhang, Z. Jiang, X. Li, Understanding oxygen vacancies in disorder-engineered surface and subsurface of $CaTiO_3$ nanosheets on photocatalytic hydrogen evolution, Appl. Catal. B Environ. 267 (2020), 118378, https://doi.org/10.1016/j.apcatb.2019.118378.
[60] X. Pan, M.Q. Yang, X. Fu, N. Zhang, Y.J. Xu, Defective TiO_2 with oxygen vacancies: synthesis, properties and photocatalytic applications, Nanoscale 5 (2013) 3601–3614, https://doi.org/10.1039/c3nr00476g.
[61] Y. Yang, L.-C. Yin, Y. Gong, P. Niu, J.-Q. Wang, L. Gu, X. Chen, G. Liu, L. Wang, H.-M. Cheng, An unusual strong visible-light absorption band in red anatase TiO_2 photocatalyst induced by atomic hydrogen-occupied oxygen vacancies, Adv. Mater. 30 (6) (2018) 1704479.